Title
Characterisation of residual stresses in heat treated, high strength aluminium alloy extrusions

Journal
Materials Science and Technology, 32(14)

ISSN
0267-0836

Authors
Olson, MD
Robinson, JS
Wimpory, RC
et al.

Publication Date
2016-09-21

DOI
10.1080/02670836.2016.1164973

Peer reviewed

Characterisation of residual stresses in heat treated, high strength aluminium alloy extrusions

Mitchell D. Olson[1*], Jeremy S. Robinson[2], Robert C. Wimpory[3], and Michael R. Hill[4]

[1]*Hill Engineering, LLC, 3035 Prospect Park, Rancho Cordova, CA, USA*
[2]*Department of Mechanical, Aeronautical and Biomedical Engineering, University of Limerick, Ireland*
[3]*Helmholtz-Zentrum Berlin for Materials and Energy, Hahn Meitner Platz 1, Berlin, Germany*
[4]*Department of Mechanical and Aerospace Engineering, University of California, One Shields Avenue, Davis, CA, USA*

Submitted to *Materials Science and Technology*, January 2016

ABSTRACT

Residual stresses were measured in rectilinear aluminium bars quenched using an aqueous polyoxyethylene glycol (PAG) solution or cold-water. Residual stresses were measured with neutron diffraction and a superposition based method using mechanical strain release measurements. Three orthogonal stress components were measured along two transverse lines using neutron diffraction. The longitudinal residual stresses were mapped over a transverse cross section using the contour technique. A primary slice removal technique mapped three orthogonal residual stresses over a transverse cross section in the PAG extrusion. Residual stresses were found to vary from biaxial compressive in the part boundaries to triaxial tensile in the interiors. There was close correlation between the neutron diffraction and mechanical strain release techniques. PAG quenching demonstrated lower residual stresses.

Keywords: Residual stress; quenching; aluminium alloy; PAG quenching; cold water quenching; 7050; contour technique; primary slice removal mapping

1. INTRODUCTION

Aluminium alloys have been the dominant aerospace structural material since Alfred Wilm discovered precipitation hardening in 1906.[1, 2] This era now appears to be coming to a close, as composites are finding use for fuselage, wing, and empennage of large passenger aircraft. However, aluminium continues to be an outstanding material choice for many structural applications.[3, 4] This is especially true where its isotropy and performance in compression can be exploited.[5] 7050 is one of the established aluminium alloys that has been used in many aircraft components. Available in most product forms, the alloy was developed with improved resistance to stress corrosion cracking and low quench sensitivity in mind so that it could be used for both thick plate and forging applications.[6]

All aerospace aluminium alloys are heat treated as part of the precipitation hardening process. The critical step is rapid quenching to produce a super saturated solid solution that can be subject to a controlled decomposition known as aging. Thermal gradients induce non-uniform plastic deformation during quenching which result in large magnitude residual stresses. A variety of methods exist to minimize the impact of these residual stresses.[7] For semi-finished product forms, these revolve around the application of plastic deformation by stretching or cold compression. For complex geometries, it is

* Corresponding author. *E-mail address:* molson@hill-engineering.com

more difficult to plastically deform the product so the thermal gradients must be managed by using less aggressive quenching regimes. The most common quenchant, after water, is an aqueous solution of polyoxyethylene glycol known as PAG or polymer. PAG was introduced in the 1960s and is now established as the most effective route to reduced distortion in slender shaped products.[8-10] PAG has an inverse solubility in water and when the temperature exceeds ~70°C it is precipitated from solution. When quenching into a solution of PAG, a film is formed around the work piece. It is the more uniform heat transfer through this film and the increased ease of rewetting of the aluminium surface that is reported to result in reduced residual stress and distortion.[11] The thickness of the polymer film will depend on the solution heat treatment temperature, the concentration of PAG, the relative heat capacities of the piece and the quenchant, and the temperature of the quenchant. For a given work piece geometry, the concentration of PAG can be varied to alter the cooling rate between a boiling water quench and a cold water quench. PAG successfully lowers residual stress and subsequent distortion while maintaining acceptable mechanical properties when compared to water quenching (T<60°C).[12] PAG type products are increasingly popular for quenching of thin section or complex shapes where mechanical methods of stress relief are not applicable and hot or boiling water quenching would result in too great a reduction in mechanical properties. The reduction in strength associated with PAG quenching is a function of many variables but is illustrated in Fig. 1 for 7075 aluminium rectilinear forgings. The tensile properties arising from quenching into three PAG concentrations at 30°C are compared to cold water and boiling water quenched properties.[13] 7075 aluminium is a quench sensitive alloy, as demonstrated by the large loss in strength exhibited in the boiling water quenched forging. In contrast, the PAG quenched forgings suffered a far smaller drop in strength for both the 25 and 100 mm thick forgings especially at the lower concentrations. Commercial practice usually results in at least two concentrations of PAG being offered. Thin gauge or slender shaped products typically use PAG quenchants at a concentration of 25-40% while for heavy section forgings it is 10-20%. Recent developments of PAG type media include alternative quenchants that can be used at higher temperatures and lower concentrations to lessen the environmental impact.[14]

As previous work has shown, PAG and cold water quenching can result in materials that exhibit similar strength levels, but the differences in the resulting residual stresses have not been fully researched. In this investigation, we wish to determine the difference in the final residual stress state for both a 16% PAG concentration and cold water quenching as a function of all three normal stress components. To do so, measurements have been made with neutron diffraction and a relatively new mapping technique using mechanical stress release measurements and superposition, called primary slice removal (PSR) mapping. The PSR mapping measurement in this paper is the most comprehensive to date, since it measures all three orthogonal stress components. From a practical engineering perspective, the use of both diffraction and mechanical measurement techniques provides confirmatory data, and confidence in the measured stresses. Furthermore, the neutron diffraction residual stress measurements provide a means to validate the new PSR mapping technique, and builds on previous validation efforts.[15, 16]

2. METHODS

2.1. Sample description

Measurements were performed on two aluminium bars that were cut from 50.8 mm (2 in) thick and 76.2 mm wide 7050 aluminium extrusions. The original length of both bars was 609.6 mm (24 in). Each bar was received in the T7451 condition, being stress relieved by stretching and then over aged. To introduce a higher residual stress state, both bars underwent a subsequent solution heat treatment of 3

hours at 477 °C followed by immersion quenching into a room temperature quenchant. Each bar used a different quenchant; one bar used normal water and will be notated as the cold water quench (CWQ) bar, and the other bar was quenched into an aqueous solution of 16% polyoxyethylene glycol (PAG) (Aqua-Quench 260, Houghton International Inc.) and will be notated as the PAG quenched bar. The additional over aging treatment was representative of that used for the T74 temper[17], and consisted of a dual artificial age at 121°C for 8 hours followed by 177°C for 8 hours. A recent investigation has shown that stress relief will not occur at the initial aging temperature of 121°C, but will take place at 177°C.[18] The amount of stress relief caused by over aging will be in the range 20-35% but in this study, both extrusions will be similarly affected.

The coordinate system used for residual stress measurement has an origin at the bottom left hand corner of the bar cross section at the mid-length of the bar, with positive *x* along the 76.2 mm width, to the right (the long transverse, LT dimension of the extrusion), positive *y* along the 50.8 mm thickness (the short transverse, ST dimension of the extrusion), and positive *z* along the length of the bar (the longitudinal, L dimension of the extrusion), as shown in Fig. 2.

The microstructure of the PAG quenched bar consisted of long, rod like grains as shown in Fig. 3. The cross-section of the grains in the short-long transverse plane were approximately 75 μm in the long transverse direction and 100 μm in the short transverse direction. The grains were very long in the extrusion direction, around 500-1000 μm. The grains contained a substructure and both sub grain and grain boundaries were decorated with fine second phase $MgZn_2$ (η) precipitates formed during quenching. The intragranular precipitates arising from aging were not resolvable in the optical microscope.

2.2. Primary slice removal mapping measurements

The goal of the primary slice removal mapping measurements is to determine multiple components of the residual stress along a selected measurement plane. Since there are several part configurations, Fig. 4 shows the stress decomposition of the initial stress into each part that is measured. The nomenclature used to denote the stress in each part configuration, is given as $\sigma(x, y, z)$, with a superscript notating the configuration (A, B, C) or the stress release (*i*, *ii*), for all stress components, at the specified spatial location (x, y, z). With the given nomenclature, the goal of the biaxial mapping measurements can be more precisely stated as measuring $\sigma^A_{xx}(x, y, z)$, $\sigma^A_{yy}(x, y, z)$, and $\sigma^A_{zz}(x, y, z)$ at the plane of interest ($z = 0$). The theoretical background of PSR mapping was initially published in[15] and a summary is given here.

The biaxial mapping measurement consists of several steps and is graphically summarized in Fig. 4. The measurement steps consist of cutting the bar in half, changing the bar from the initial configuration (configuration A in Fig. 4) to a half bar (configuration B in Fig. 4). During the configuration change from A to B, stress was released and is denoted as $\sigma^i(x, y, z)$, which was measured with the contour method. The next step is to remove several thin-slices adjacent to the contour method measurement, as is shown in configuration C in Fig. 4. The stress released during the configuration change from B to C, $\sigma^{ii}(x, y, z)$, is not directly determined as will be described below. Stress in configuration C is determined using slitting (aka, incremental slitting, crack compliance method). With all the configuration changes described, the superposition used to determine the initial stress is

$$\sigma^A(x, y, 0) = \sigma^i(x, y, 0) + \sigma^B(x, y, 0) = \sigma^i(x, y, 0) + \sigma^{ii}(x, y, 0) + \sigma^C(x, y, 0). \quad (1)$$

A diagram of the all the sectioning steps is shown in Fig. 5 to more easily understand the configuration changes.

For parts where the out-of-plane stress (σ^A_{zz}) does not vary with the out-of-plane direction, the stress in the initial configuration can be decomposed[15] into

$$\sigma^A(x, y, 0) = \sigma^{A(z)}(x, y, 0) + \sigma^C(x, y, 0) \quad (2)$$

where $\sigma^{A(z)}$ is a theoretical construct that gives the change in stress that would occur in a thin slice removed from a part, which would cause the release of the out-of-plane stresses in the slice. This stress is the sum of σ^i and σ^{ii}, and will be notated as the primary slice removal stress. To determine the primary slice removal stress only $\sigma^i_{zz}(x, y, 0)$ and $\sigma^{ii}_{zz}(x, y, 0)$ will be needed, since only the out-of-plane stress components are needed to determine $\sigma^{A(z)}$.

2.2.1. Contour method measurements, σ^i

The release stress, $\sigma^i_{zz}(x, y, 0)$ is measured with the contour method. Theoretical background for the contour method can be found in[19] and the experimental details for these aluminium bars are given below.

At each contour measurement plane, the bar was sectioned in half using a wire EDM on a low power setting designed for finishing cutting. While cutting the sample, it was rigidly clamped to the EDM frame. After cutting, the surface height profile as a function of in-plane position was measured using a laser scanning profilometer for each section. The measurement spacing of the surface profile was on a 200 μm grid. The two surface profiles were then averaged and fitted to a smooth analytical function. The level of smoothing was selected by choosing the number of terms in the analytical function during data reduction.

The negative (mirror image) of the smoothed, averaged surface profile was then applied as a displacement boundary condition to a linear elastic finite element model of the cut specimen. The finite element mesh used eight-node, linear interpolation brick elements with a node spacing of 1 mm along the cut plane with a bias mesh away from the cut plane. The mesh was sufficiently refined such that when the node spacing is reduced there is negligible change in stress. A Young's modulus (E) of 71.0 GPa and a Poisson's ratio (ν) of 0.33 were used in the finite element model.[20, 21]

Three contour measurements were made in the CWQ and five were made in the PAG quenched bars and the measurement locations are shown in Fig. 2. The first contour method measurement in both bars cut the bar at the mid-length (plane 1, z = 0), followed by contour measurements at the mid-length of each of the remaining half bars (planes 2A, 2B, z = -152.4 mm, 152.4 mm). For the PAG quenched bar, two additional contour measurements were made at the mid-length of two of the quarter bars (planes 3A, 3B, z = 76.2 mm, 228.6 mm). The distance between measurements is such that there is no effect of previous measurements on subsequent measurements (confirmed in the contour method results in previous measurements). Only the PAG quenched bars were used to complete the in-plane stress mapping measurements (the CWQ bar measurements concluded with the three contour method measurements; therefore only the σ_{zz} component of residual stress was captured for the CWQ extrusion).

In addition to determining $\sigma^i_{zz}(x, y, z)$ during the contour method stress calculation step, all normal components of $\sigma^i(x, y, z)$ are automatically determined (i.e., $\sigma^i_{xx}(x, y, z)$, $\sigma^i_{yy}(x, y, z)$, $\sigma^i_{zz}(x, y, z)$) at all spatial locations in the bar. This is because the contour method cut will release some in-plane stresses due to a Poisson effect and this will contribute to the surface profile measured to calculate stress.

Similarly, the in-plane stress release is also quantified in the finite element model used to calculate the out-of-plane stress release, since the stress release from both the in-plane and out-of-plane components contribute to the measured surface profile.

2.2.2. *Primary slice removal stress, $\sigma^{A(z)}$*

To determine $\sigma^{A(z)}$, both $\sigma^{i}_{zz}(x, y, 0)$ and $\sigma^{ii}_{zz}(x, y, 0)$ are needed. However, during the σ^{i} measurement, a stress-free surface was created at $z = 0$, which forces σ_{zz} in all subsequent configurations and stress release steps to be zero. Therefore, only $\sigma^{i}_{zz}(x, y, 0)$ is needed to determine $\sigma^{A(z)}$.

The finite element simulation used to compute the primary slice removal stress used the same geometry of the slices in configuration C, but with half-thickness symmetry. The total out of plane stress, as was determined as $\sigma^{i}_{zz}(x, y, 0)$ was applied as a traction boundary condition on the face of the slice and the resulting stress after equilibrium gives $\sigma^{A(z)}$. The analysis used a mesh consisting of eight-node, linear interpolation brick elements with a global node spacing of 0.5 mm, which resulted in six elements through the slice thickness for a total of roughly 78,000 elements. The mesh was sufficiently refined such that when the node spacing is reduced there is negligible change in stress. The analysis used the earlier stated elastic material properties.

2.2.3. *Slitting measurements*

Slitting was used to determine the stress remaining in the slices of configuration C. In total eleven slices were used to determine σ^{C}_{xx} and five slices were used to determine σ^{C}_{yy}, with each slitting measurement line shown in Fig. 7. All slices were 6.35 mm (0.25 in) thick and eight slices were removed from each side of the plane of interest using a wire EDM.

Only one slitting measurement was made on each slice. The measurements consisted of adhering a strain gauge (gauge length of 1.5 mm) on the back face of the slitting measurement plane, incrementally cutting a slit into the slice, and measuring the resulting strain after each cut increment. The slit cut all through the slice thickness in the *z*-direction. For σ^{C}_{xx}, cutting started at $y = 0$ and ended at $y = 71.12$ mm with measurements at $x = 6.35$, 12.7, 19.05, 25.4, 31.75, 38.1, 44.45, 50.8, 57.15, 63.5, 69.85 mm (Fig. 7); similarly σ^{C}_{yy} cutting started at $x = 0$ and ended at $x = 47.498$ mm with measurements at $y = 19.05$, 25.4, 31.75, 38.1, 44.45 mm (Fig. 7). Using the strain versus cut depth data, stress is calculated using an elastic inverse[22], with Tikhonov regularization[23] to minimize the effect of noise in the data.

2.3. *Neutron diffraction*

Measurements were made following the guidelines present in recently published papers.[24-26] Neutron diffraction was performed on the strain scanning instrument, E3 (HZB, Wannsee, Berlin, Germany). A sampling gauge volume of 5 x 5 x 2 mm^3 was used. The relatively large gauge volume was required to counter crystallographic texture limiting the diffracted intensity of the peak in certain measurement directions. The gauge volume was defined by the incident beam slit width (5 mm), slit height (5 mm), and the diffracted beam radial collimators (2 mm). The extrusions were positioned on the instrument stage to permit measurements of strains in the three primary working orthogonal directions. These directions were assumed to be the principal stress directions, being coincident with the direction of maximum heat flow out of the extrusion surfaces during quenching. The strain measurements originated from the vertex at the centre of the 146 mm (longitudinal, *L*, *z*) x 76 mm (long transverse, *LT*, *x*) x 52 mm (short transverse, *ST*, *y*) extrusions, moving out to the surfaces in the LT and ST directions only (i.e., measurements were made in the *x*-*y* plane). Strain measurements were made at 15 points along a

line in the LT direction and 11 along in a line in the ST direction. Nine strain free reference cubes with a side length of 5 mm were extracted from the end faces of each extrusion by electro-discharge machining. The {311} peak positions were converted to residual strains and then to stresses using the standard three-dimensional Hooke's law.[27] A Young's modulus (E) of 70.0 GPa and a Poisson's ratio (ν) of 0.3 were used in all the calculations. Multiple (repeatability) neutron diffraction measurements on the blocks and the associated stress free samples allowed an estimation of one standard deviation random uncertainties as ±30 MPa. These uncertainties were typically larger than the statistical errors arising from peak fitting which are shown in the figures below.

3. RESULTS

The longitudinal stress, σ_{zz}, in the CWQ bar measured with the contour method can be seen in Fig. 9, which includes the measurements from all three cuts and the mean. The results show all three measurements are very similar, with large compressive stresses along the boundary of the part with a minimum around –200 MPa and with tensile stresses in the part interior with a maximum around 225 MPa. Line plots of the longitudinal stress in the CWQ bar measured with the contour method and neutron diffraction are shown in Fig. 10. The line plots better illustrate the stress distribution present in the bar; where along the *x*-direction the stress has a roughly parabolic distribution and along the *y*-direction the stress has a roughly sinusoidal distribution. The line plots show the magnitude of the compressive stress is larger at the *x*-direction edges (minimum of -200 MPa) compared with the *y*-direction edges (minimum of -100 MPa). Results from the two residual stress measurement techniques are in good agreement.

The longitudinal stress, σ_{zz}, in the PAG quenched bar measured with the contour method can be seen in Fig. 11, which includes all five measurements and the mean. The results show all five measurements are very similar, with large compressive stresses along the boundary of the part with a minimum around -175 MPa and with tensile stresses in the part interior with a maximum around 175 MPa. Line plots of the longitudinal stress in the PAG quenched bar measured with the contour method and neutron diffraction are shown in Fig. 12. The stress distribution present in the PAG bar also has a roughly parabolic distribution in the *x*-direction and a roughly sinusoidal distribution in the *y*-direction. The line plots also illustrate that the magnitude of the compressive stress is larger at the *x*-directions edges (minimum of -175 MPa) compared with the *y*-direction edges (minimum of -100 MPa). The residual stress magnitude in the PAG quenched bar has been reduced 14% and 18% compared to the CWQ bar using the contour method measurements (average of all spatial locations) and neutron diffraction measurements, respectively.

The long transverse stress, σ_{xx}, found with PSR mapping in the PAG quenched bar is shown in Fig. 13. The stress remaining in the slice, σ^{C}_{xx}, has compressive stresses along the boundary of the measurement area with a minimum around -90 MPa and tensile stresses in the part interior with a maximum around 70 MPa. The primary slice removal stress, $\sigma^{A(z)}_{xx}$, has a similar distribution, but with lower magnitudes. The minimum compressive stress along the part boundary is -25 MPa and the maximum tensile toward the part interior is 30 MPa. The stress in the initial part configuration, σ^{A}_{xx}, also has compressive stresses along the boundary of the measurement area with a minimum around -115 MPa and tensile stresses in the part interior with a maximum around 100 MPa. Line plots of the long transverse stress in the PAG quenched bar measured with PSR mapping and neutron diffraction are shown in Fig. 14. Similar to the longitudinal stress, the stress distribution in the long-transverse direction also has a relatively flat parabolic distribution in the *x*-direction and a roughly sinusoidal

distribution in the *y*-direction. The line plots show that the stress distribution has a strong spatial dependence.

The short transverse stress, σ_{yy}, found with PSR mapping in the PAG quenched bar is shown in Fig. 15. The stress remaining in the slice, σ^{C}_{yy}, has compressive stresses along the boundary of the measurement area with a minimum around -155 MPa and tensile stresses in the part interior with a maximum around 20 MPa. The primary slice removal stress, $\sigma^{A(z)}_{yy}$, has a somewhat similar distribution, but with lower magnitudes, with a minimum compressive stress along the part boundary of -15 MPa and a maximum tensile stress toward the part interior at 10 MPa. The stress in the initial part configuration, σ^{A}_{yy}, also has compressive stresses along the boundary of the measurement area with a minimum around -175 MPa and tensile stresses in the part interior with a maximum around 30 MPa. Line plots of the short transverse stress in the PAG quenched bar measured with PSR mapping and neutron diffraction are shown in Fig. 16. Different from the longitudinal and long transverse stresses, the stress distribution in the short transverse direction has a parabolic distribution toward the *x*-direction edges and is then flat over most of the interior, and also roughly flat along the *y*-direction.

These measurements also provide the opportunity to compare the residual stress using different quenchants. A comparison between the CWQ and the PAG quenched bars for the longitudinal stress, σ^{A}_{zz}, can be seen in Fig. 17. As would be expected the stresses in the PAG quenched bar have lower magnitudes.[28]. It is interesting that the measured longitudinal stresses along the part boundary show similar levels of compressive stress around -200 MPa. A comparison of the long transverse stress, σ^{A}_{xx}, can be seen in Fig. 18 and of the short transverse stress, σ^{A}_{yy}, in Fig. 19. Both measured stress components in the PAG quenched bar have systematically lower magnitudes than found in the CWQ bar. For the long transverse stress, σ_{xx}, the neutron diffraction measurements show a 24% reduction in residual stress magnitude between the PAG and cold-water quenched bars on average. For the short transverse stress, σ_{yy}, the neutron diffraction measurements show essentially no reduction in residual stress magnitude between the PAG and cold-water quenched bars on average.

4. DISCUSSION

The stresses measured with PSR mapping and neutron diffraction both show stresses that are typical of quenched aluminium with large magnitude compressive stress along the part boundary and large magnitude tensile stress toward the centre of the quenched cross-section.[29-31]. One unique advantage of both PSR mapping and neutron diffraction is that they are able to measure multiple components of the stress tensor over a range of spatial locations. PSR is unique among all residual stress techniques that it provides a *map* of multiple stress components.

Overall the agreement between PSR mapping and neutron diffraction is very good, as is shown in the line plots of Fig. 10, Fig. 12, Fig. 14, and Fig. 16. As the plots show, both measurement techniques are capturing the same trends in the residual stress spatial distribution, with most measurements within 40 MPa of one another (the largest difference is around 100 MPa). Overall, the neutron diffraction results appear to systematically display larger magnitudes than the PSR mapping results.

The magnitude of the reduction in residual stress caused by quenching into PAG as determined here (14 to 18% for the longitudinal stress) is smaller than would be expected from the literature. Other investigations suggest up to a 45% reduction in residual stress is possible for a 16% PAG concentration.[32, 33]. However, there are other factors that can influence the efficacy of the PAG quench including sample size, immersion rate, agitation of the quenchant, maintenance of the quenchant chemistry.

The choice of appropriate elastic constants for the calculation of stress from strain is important. For neutron diffraction the specific values for each crystallographic direction can vary immensely, depending on the elastic anisotropy of the material. Pure aluminium has very low elastic anisotropy, implying values close to the bulk values are expected. For instance, pure aluminium has a bulk Young's Modulus of E=70.6 GPa, and Poisson's ratio of ν=0.345.[34] The corresponding specific values (for all reported interatomic planes) vary over a small range E_{hkl} = 67-73 GPa and ν_{hkl} = 0.35-0.36 both being close to the bulk value.[35]Aluminium alloys appear to have a similar bulk Young's modulus to pure aluminium but smaller values for Poisson's ratio. Assuming the alloys also have a low elastic anisotropy, then the corresponding specific ν_{hkl} values should also have lower values. Measured values for 7050 using neutron diffraction report E_{311} = 71.1 GPa and ν_{311} = 0.34.[36] Bulk values for 7050 provide values of E = 70 GPa and ν = 0.33.[37, 38]

Depending on the values of strain, differences in the value of the Poisson's ratio can make a significant difference. Using the example of the longitudinal stress value at y = 25mm (Fig. 12b), the neutron strain values are ε_{zz} (L) = 2202 ± 81, ε_{xx} (LT) = 830 ± 186 and ε_{yy} (ST) = -1014 ± 144 µm/m. Using moduli values of E_{311} = 70 GPa and ν_{311} = 0.33 would give a longitudinal σ_{zz} (L) stress value of 219 ± 15 MPa, whereas using values of E_{311} = 71.1 GPa and ν_{311} = 0.34 would give a longitudinal stress value of 231 ± 16 MPa. It is therefore important to find the most appropriate value of elastic constants for the particular material. If values are hard to obtain, then measuring the elastic constants in-situ in a stress rig could be a possibility. In this investigation E=70 GPa and ν = 0.3 were used for the neutron diffraction calculations. These elastic constants have been found by the authors to offer the best agreement between neutron diffraction and other residual stress measurement techniques, including x-ray diffraction, incremental centre hole drilling and deep hole drilling for 7000 series alloys.

5. SUMMARY/CONCLUSIONS

Residual stresses were measured in two aluminium bars using different quenchants. One used cold water and the other a PAG solution. All three normal stress components over a cross-sectional plane were measured with both neutron diffraction and a relatively new superposition based method using a series of mechanical strain release measurements that is called primary slice removal mapping.

The measured residual stresses found from PSR mapping and neutron diffraction are in general agreement, with the neutron diffraction measuring somewhat larger magnitudes than the stresses measured with PSR mapping. The results show the stresses in the PAG quenched bars have systematically lower residual stresses. The stress in all three normal components has compressive stress along the part boundary and tensile stress toward the centre of the part.

The longitudinal stress, σ_{zz}, has a parabolic distribution along the x-direction and a sinusoidal distribution along the y-direction, where the stresses range from –200 MPa (part boundary) to 225 MPa (part centre) in the CWQ bar and from –175 MPa (part boundary) to 175 MPa (part centre) in the PAG quenched bar.

The long transverse stress, σ_{xx}, has a relatively flat parabolic distribution along the x-direction and a sinusoidal distribution along the y-direction, where the stresses range from –100 MPa (part boundary) to 200 MPa (part centre) in the CWQ bar and from –50 MPa (part boundary) to 125 MPa (part centre) in the PAG quenched bar.

The short transverse stress, σ_{yy}, has a relatively flat parabolic distribution along the *x*-direction and a very flat distribution along the *y*-direction, where the stresses range from –25 MPa (part boundary) to 150 MPa (part centre) in the CWQ bar and from –75 MPa (part boundary) to 100 MPa (part centre) in the PAG quenched bar.

6. ACKNOWLEDGEMENTS

The authors acknowledge, with gratitude, the U.S. Air Force for providing financial support for portions of this work (contract FA8650- 14-C-5026). This project has received funding from the European Union's Seventh Framework Programme for research, technological development and demonstration under the NMI3-II Grant number 283883**.**

FIGURES

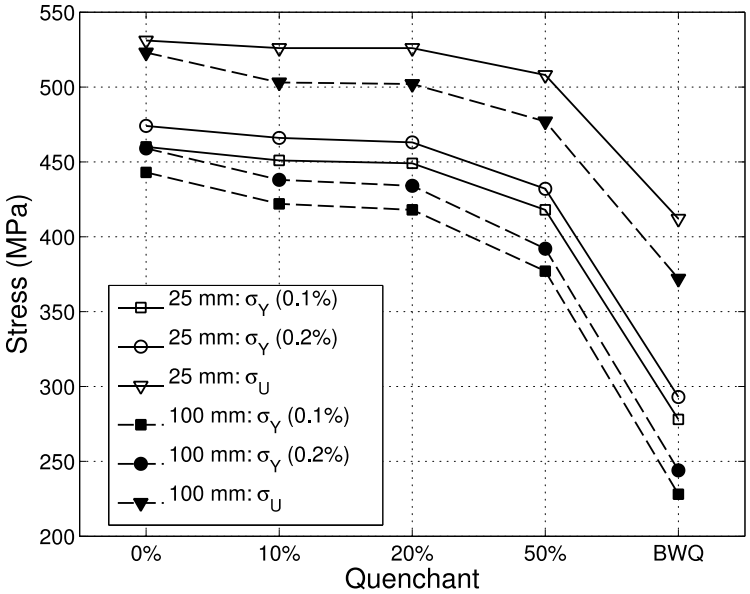

Fig. 1 – Effect of concentration of PAG quenchant upon the short transverse 0.1% and 0.2% yield strength and ultimate tensile strength of 25 and 100 mm thick forgings of 7075. Solution heat treated 4 h at 460°C and aged 12 h at 135°C [12]

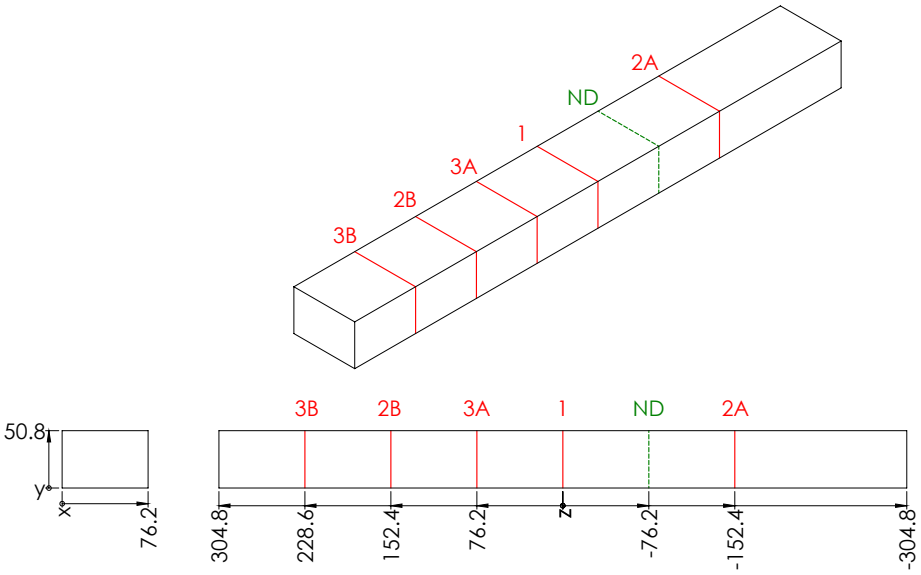

Fig. 2 – Bar dimensions and measurement locations

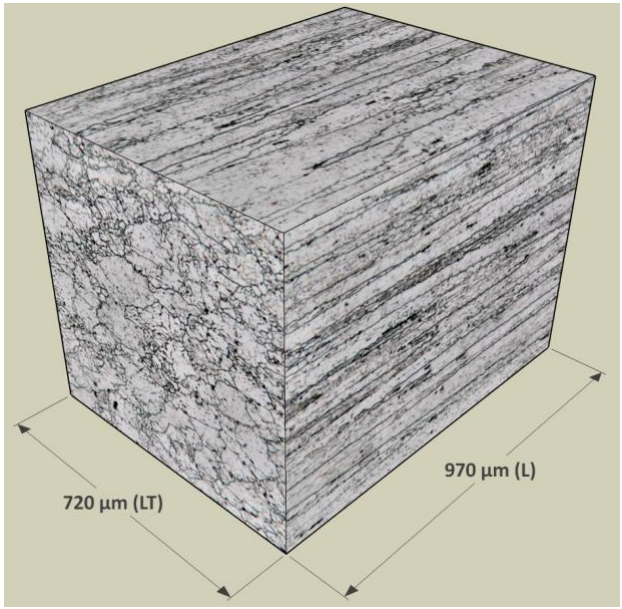

Fig. 3 – Grain structure in the PAG aluminium sample. The grains are rod like with typical cross-section dimensions of 75 µm by 100 µm with a length of 500-1000 µm

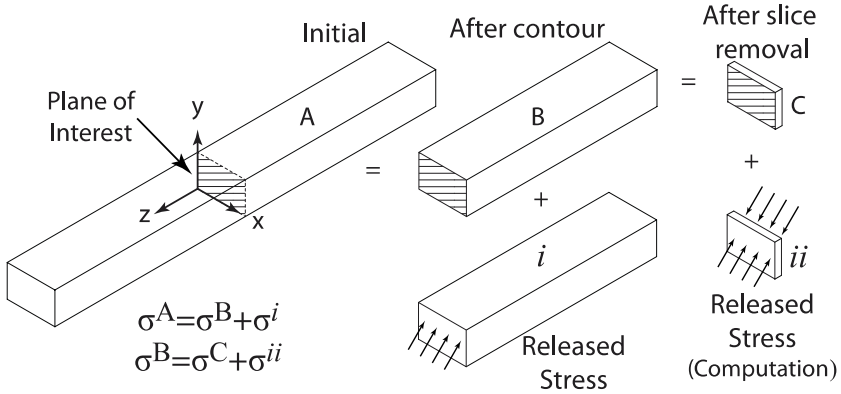

Fig. 4 – Experimental step diagram. The initial configuration (A) is cut in half to the B configuration and the stress release σ^{i} is found with the contour method. A slice (configuration C) is then removed from the B configuration. The stress release σ^{ii} is not directly found, but could be found as $\sigma^{ii} = \sigma^{A} - \sigma^{C} - \sigma^{i} = \sigma^{A(z)} - \sigma^{i}$. Plane of interest (z=0) is shown as a hatched plane

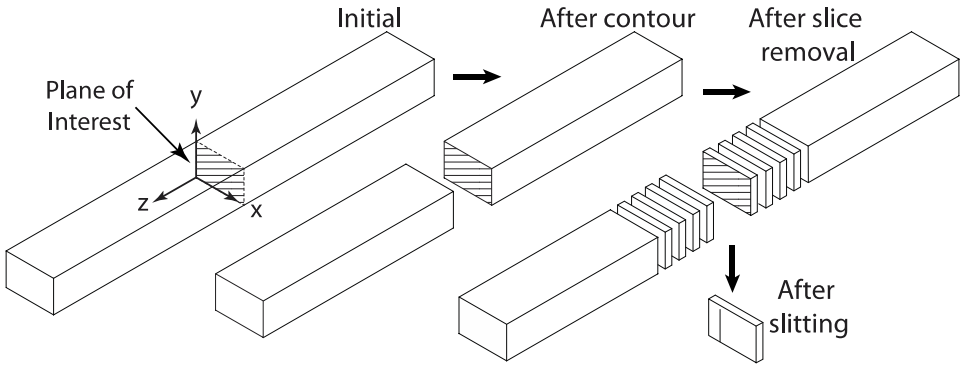

Fig. 5 – The sectioning steps used the in the biaxial mapping experiment. Plane of interest (z=0) is shown as a hatched plane

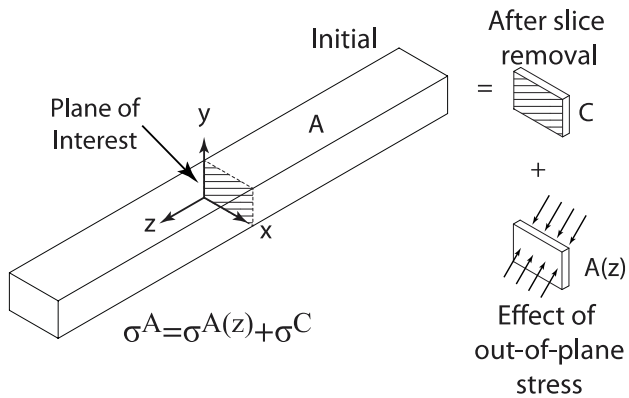

Fig. 6 – Stress decomposition diagram. The original stress (σ^A) is equal to the stress remaining in a thin slice (σ^C) plus the effect of total longitudinal stress on the thin slice ($\sigma^{A(z)}$). Plane of interest (z=0) is shown as a hatched plane

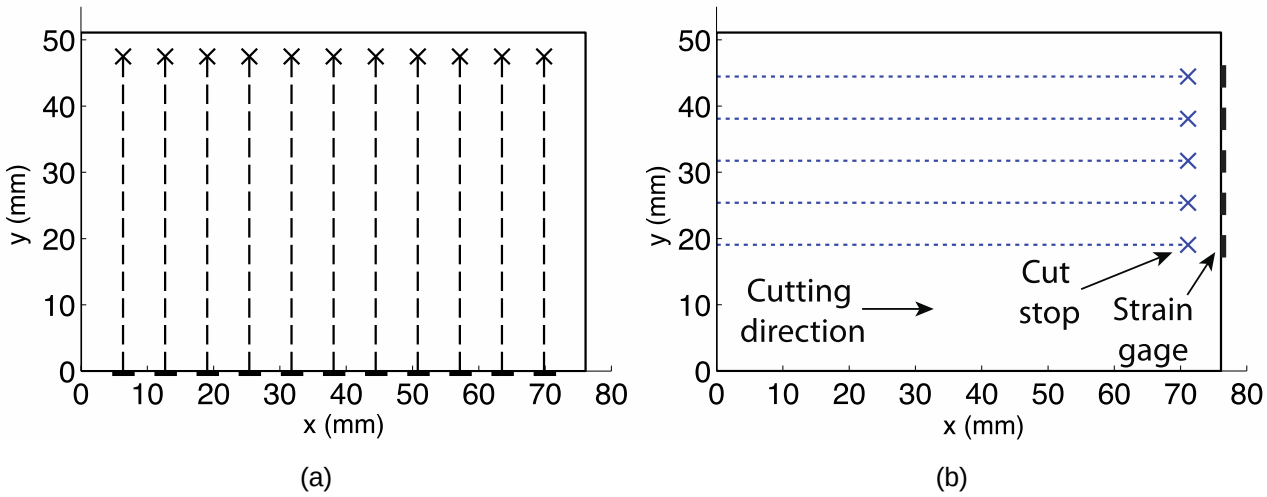

Fig. 7 – Slitting plane locations for (a) σ^C_{xx} and (b) σ^C_{yy}. Strain gauges are shown as thick lines on bottom of slice for σ^C_{xx} and on the right hand side of the slice for σ^C_{yy}. The slitting direction for σ^C_{xx} begins at the bottom of the slice and cuts towards the top and the slitting direction for σ^C_{yy} begins at the left of the slice and cuts towards the right. The maximum cut depth is indicated with an ×.

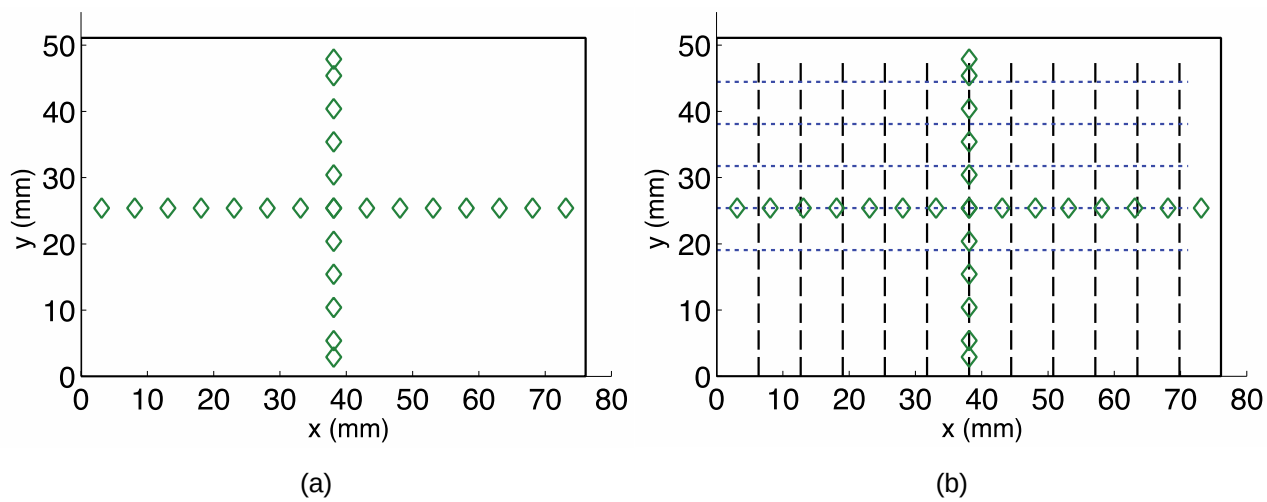

Fig. 8 – Neutron diffraction measurement point locations (a) alone and (b) shown in conjunction with the slitting locations

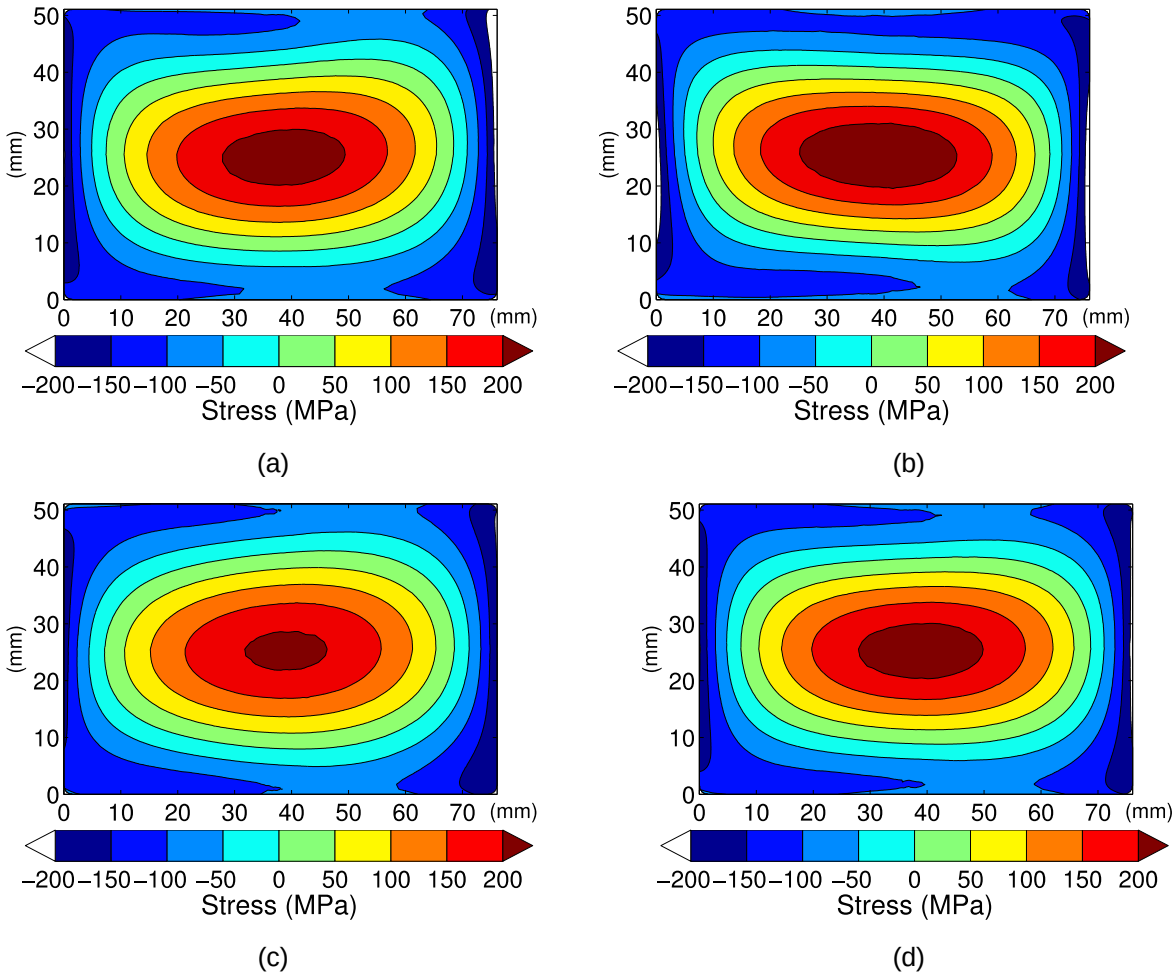

Fig. 9 – Cold water quenched contour method measurements of longitudinal stress (σ_{zz}) (a) cut 1, (b) cut 2A, (c) cut 2B, and (d) mean

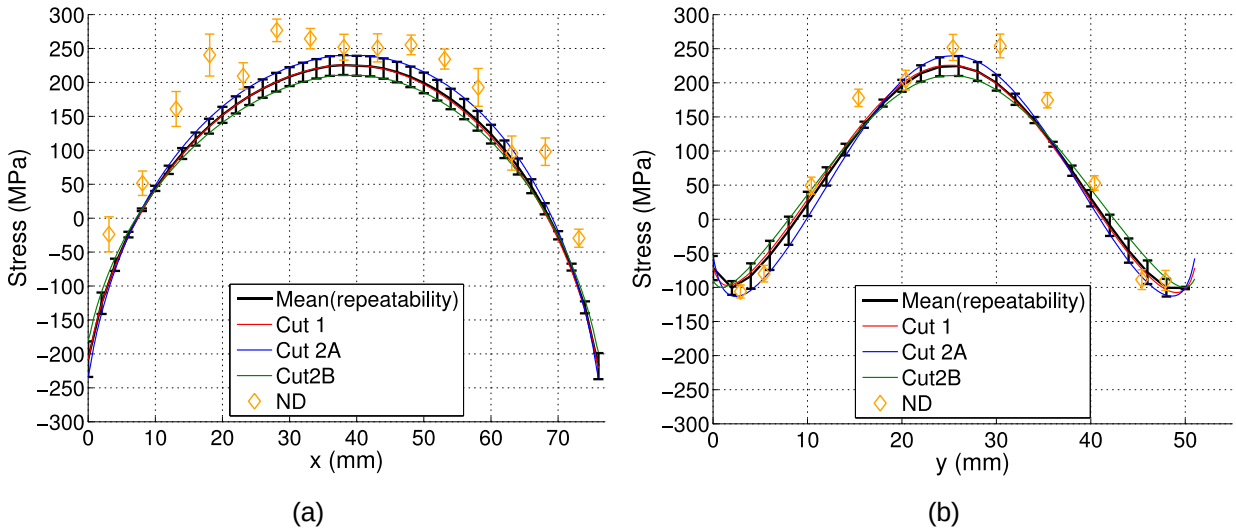

Fig. 10 – Cold water quenched longitudinal stress (σ_{zz}) line plots (a) along the x-direction at y = 38.1 mm and (b) along the y-direction at x = 25.4 mm

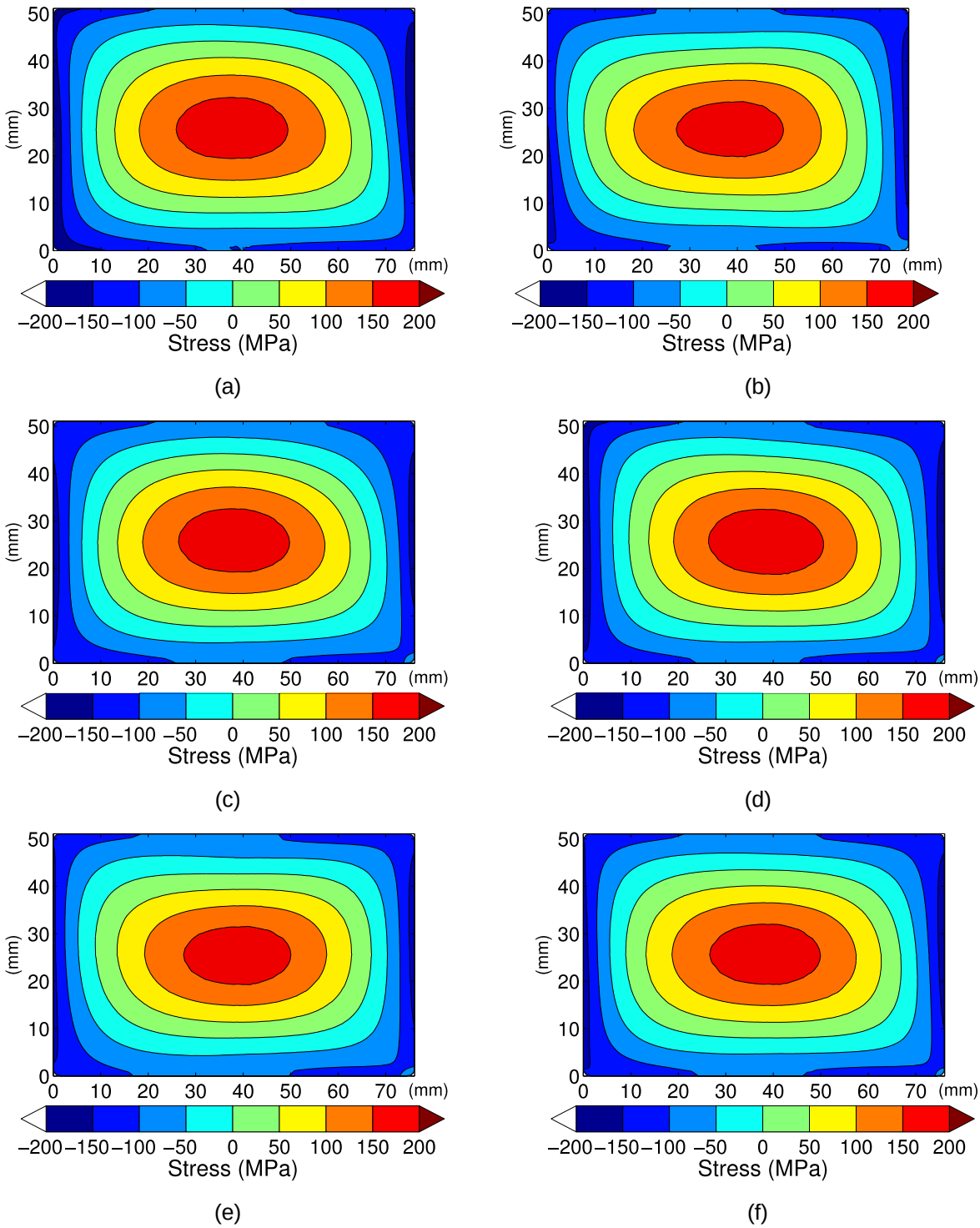

Fig. 11 – PAG quenched contour method measurements of longitudinal stress (σ_{zz}) (a) cut 1, (b) cut 2, (c) cut 3, (d) cut 4, (e) cut 5, and (f) mean

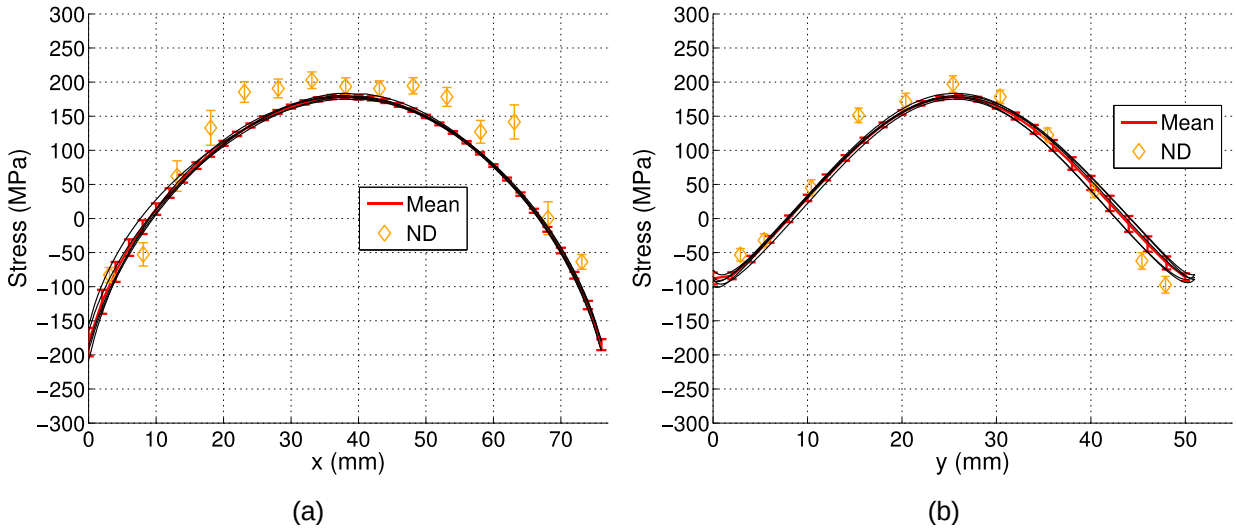

Fig. 12 – PAG quenched longitudinal stress (σ_{zz}) line plots (a) along the x-direction at y = 38.1 mm and (b) along the y-direction at x = 25.4 mm

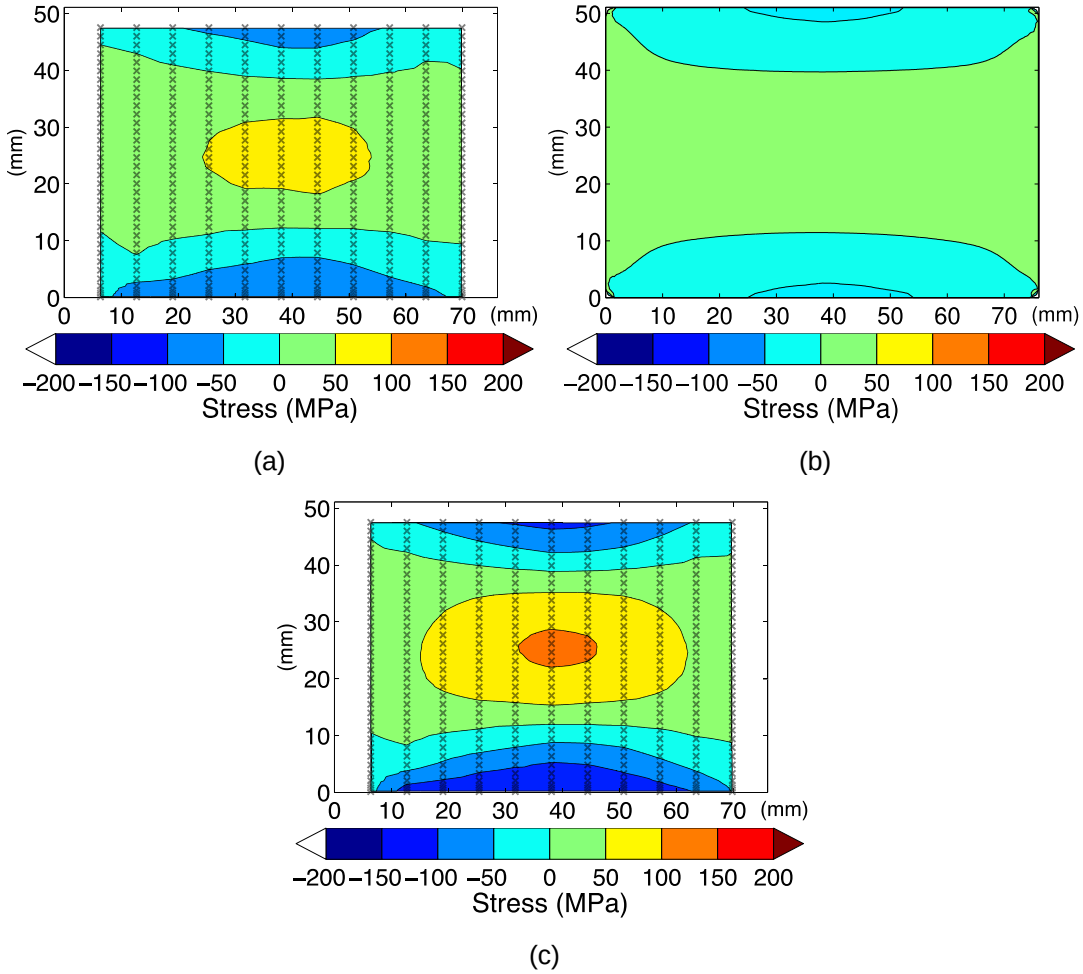

Fig. 13 – Mechanical PSR mapping measurements of the long-transverse stress (σ_{xx}) in the PAG quenched samples (a) slitting, (b) effect of the out-of-plane stress in the thin slice, and (c) total long transverse stress

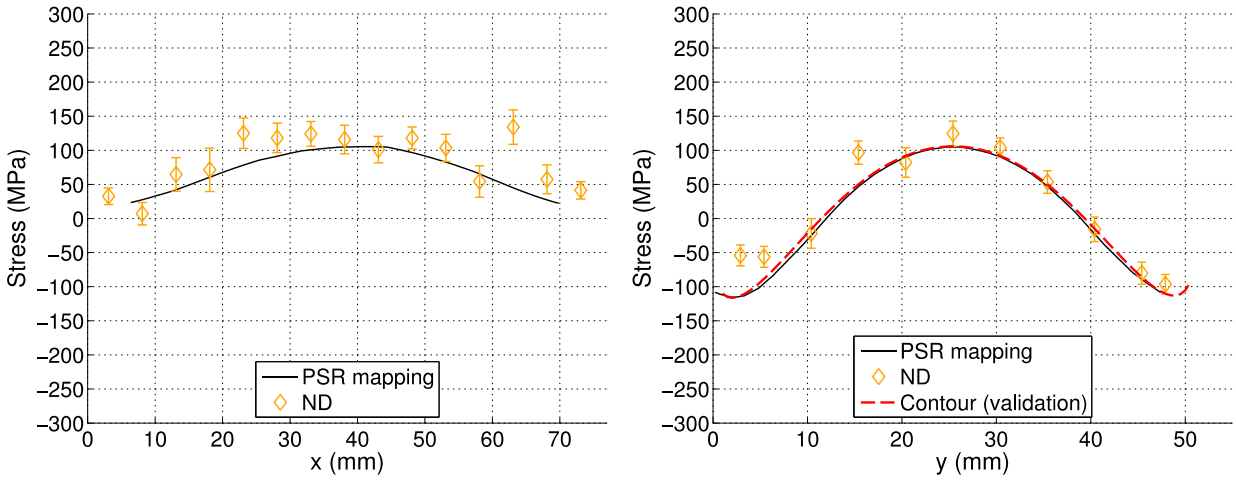

(a) (b)

Fig. 14 – PAG quenched long-transverse stress (σ_{xx}) line plots (a) along the x-direction at y = 38.1 mm and (b) along the y-direction at x = 25.4 mm

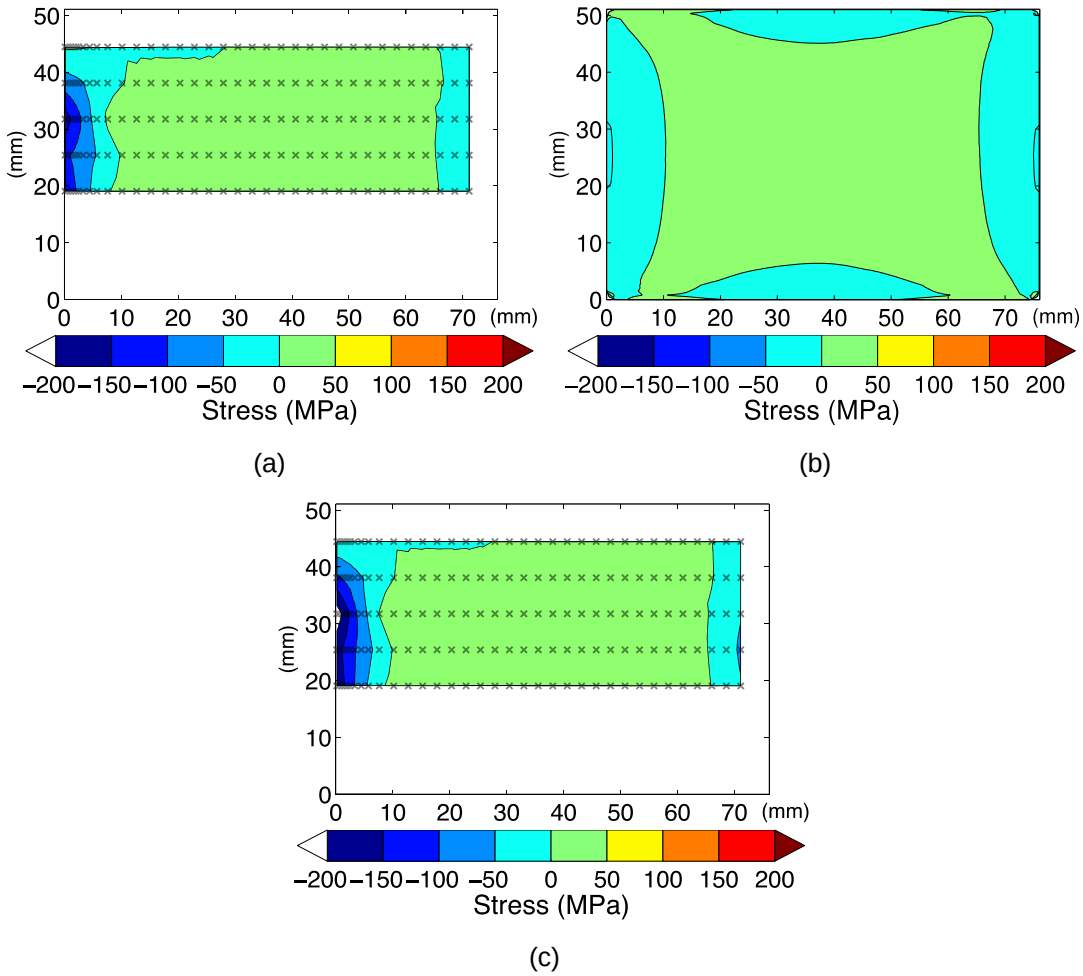

Fig. 15 – Mechanical PSR mapping measurements of the short-transverse stress (σ_{yy}) in the PAG quenched samples (a) slitting, (b) effect of the out-of-plane stress in the thin slice, and (c) total long transverse stress

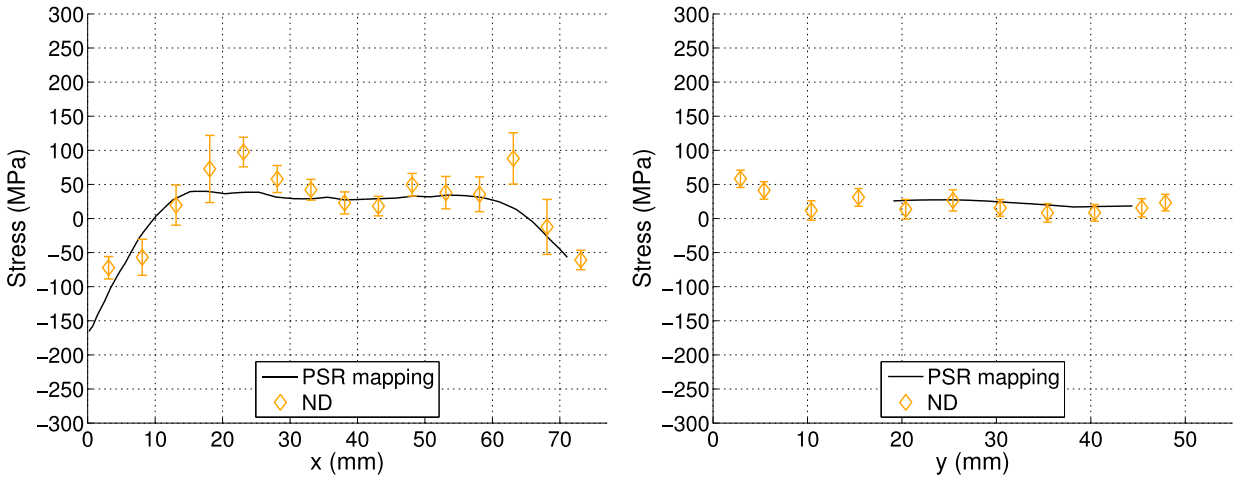

(a) (b)

Fig. 16 – PAG quenched short-transverse stress (σ_{yy}) line plots (a) along the x-direction at y = 38.1 mm and (b) along the y-direction at x = 25.4 mm

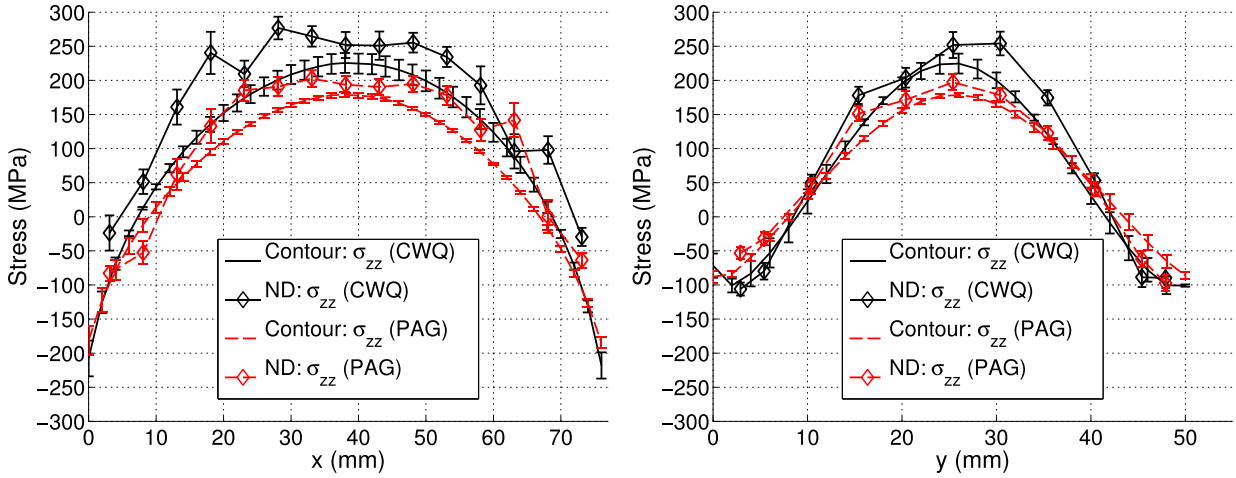

(a) (b)

Fig. 17 – Comparison of the longitudinal stress between the CWQ and PAG quenched bars measured with the contour method and neutron diffraction (a) along the x-direction at y = 38.1 mm and (b) along the y-direction at x = 25.4 mm

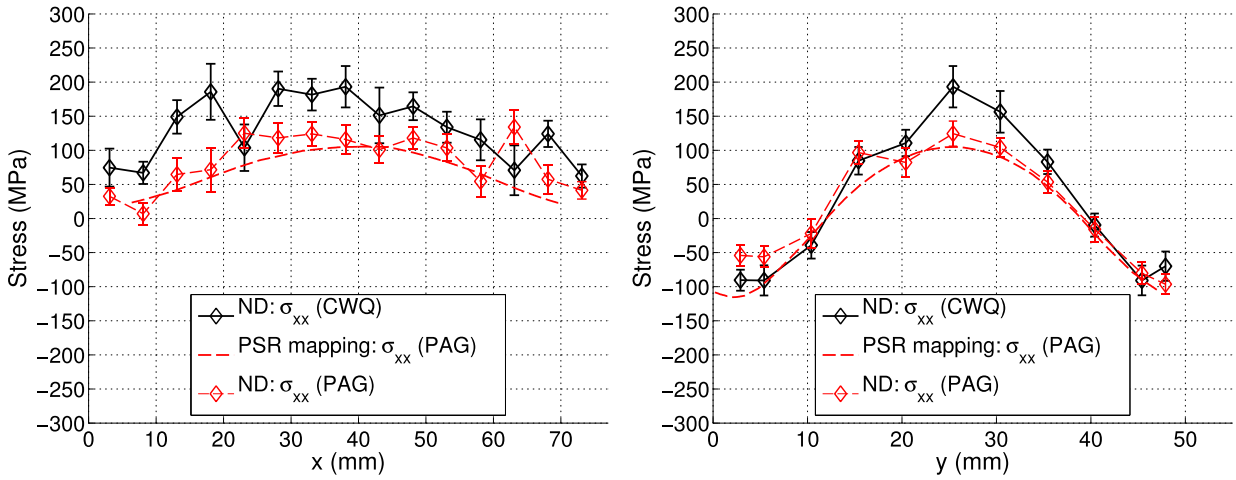

(a) (b)

Fig. 18 – Comparison of the long transverse stress between the CWQ and PAG quenched bars measured with PSR mapping and neutron diffraction (a) along the x-direction at y = 38.1 mm and (b) along the y-direction at x = 25.4 mm

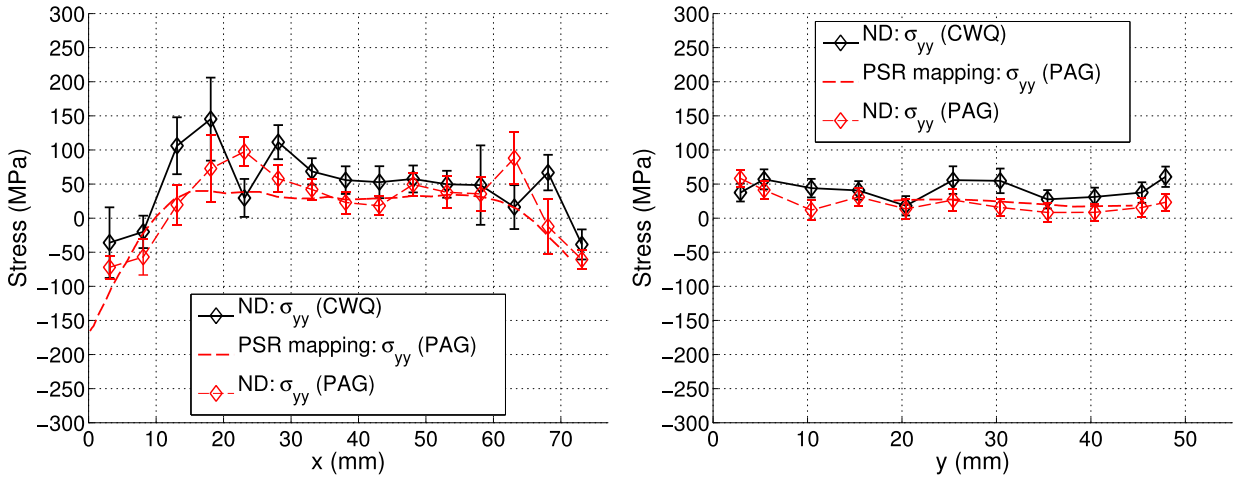

(a) (b)

Fig. 19 – Comparison of the short transverse stress between the CWQ and PAG quenched bars measured with PSR mapping and neutron diffraction (a) along the x-direction at y = 38.1 mm and (b) along the y-direction at x = 25.4 mm

REFERENCES IN MST FORMAT

1. O. Hardouin Duparc, *Rev. Met. Paris*, 2004, **101**(5), 353-360.

2. I. J. Polmear, *Materials Forum*, 2004, **28**, 1-14.

3. E. A. Starke Jr and J. T. Staley: '24 - Application of modern aluminium alloys to aircraft', in 'Fundamentals of Aluminium Metallurgy', (ed. R. Lumley), 747-783; 2011, Woodhead Publishing.

4. T. Dursun and C. Soutis, *Materials & Design*, 2014, **56**, 862-871.

5. C. J. Peel and P. J. Gregson, *Design requirements for aerospace structural materials*, in *High Performance Materials in Aerospace*, H. M. Flower, Editor. 1995, Chapman and Hall: London, UK. p. 1-48.

6. I. J. Polmear: '3 - Wrought aluminium alloys', in 'Light Alloys (Fourth Edition)', (ed. I. J. Polmear), 97-204; 2005, Oxford, Butterworth-Heinemann.

7. J. S. Robinson, D. A. Tanner, and C. E. Truman, *Strain*, 2014, **50**(3), 185-207.

8. G. E. Totten and D. S. Mackenzie: 'Aluminum quenching technology: A review', in 'Aluminium Alloys: Their Physical and Mechanical Properties, Pts 1-3', 589-594; 2000.

9. C. E. Bates and G. E. Totten, *Heat Treat. Met.*, 1988, **15**(4), 89-97.

10. T. Croucher: 'Fundamentals of quenching aluminium alloys'; 2009, Tom Croucher.

11. G. E. Totten and G. M. Webster: 'Alternatives to water quenching of aluminum alloys: A review', in '1st International Non-Ferrous Processing and Technology Conference', (eds. T. Bains, et al.), 163-173; 1997.

12. Y.-B. Dong, W.-Z. Shao, J.-T. Jiang, B.-Y. Zhang, and L. Zhen, *Journal of Materials Engineering and Performance*, 2015, **24**(6), 2256-2265.

13. R. L. Cudd: 'An assessment of UCON quenchant "A" with particular reference to its possible use in the heat treatment of aluminium alloy forgings', SX.5577, High Duty Alloys Ltd., Slough, Buckinghamshire, UK, 1969.

14. O. G. Senatorova, V. V. Sidelnikov, I. F. Mihailova, I. N. Fridlyander, A. S. Bedarev, J. I. Spector, and L. A. Tihonova: 'Low distortion quenching of aluminium alloys in polymer medium', in 'Aluminum Alloys 2002: Their Physical and Mechanical Properties Pts 1-3', 1659-1664; 2002.

15. M. D. Olson and M. R. Hill, *Exp. Mech.*, 2015, **55**(6), 1139-1150.

16. M. D. Olson, M. R. Hill, V. I. Patel, O. Muránsky, and T. Sisneros, *Journal of Nuclear Engineering and Radiation Science*, 2015, **1**(4), 041002-041002.

17. SAE, *AMS 2770. Heat Treatment Of Wrought Aluminum Alloy Parts*. 2015.

18. J. S. Robinson, C. E. Truman, T. Pirling, and T. Panzner: 'Cold Compression of the Aluminium Alloy 7075 and Associated {311} Peak Broadening', Mechanical Stress Evaluation by Neutrons and Synchrotron Radiation (MECA SENS VIII), Grenoble, France, 2015, Trans Tech Publications Ltd.

19. M. B. Prime and A. T. DeWald: 'Chapter 5. The contour method', in 'Practical Residual Stress Measurement Methods', (ed. G. S. Schajer), 2013, John Wiley & Sons.

20. Z. Zhang, Y. Yang, L. Li, B. Chen, and H. Tian, *Materials Science and Engineering: A*, 2015, **644**, 61-68.

21. MMPDS-04 : Metallic materials properties development and standardization (MMPDS)'; 2008, Washington, D.C. : Federal Aviation Administration; Columbus, Ohio : Battelle Memorial Institute ,2008:United States of America.

22. M. R. Hill: 'Chapter 4. The slitting method', in 'Practical Residual Stress Measurement Methods', (ed. G. S. Schajer), 2013, John Wiley & Sons.

23. G. S. Schajer and M. B. Prime, *J. Eng. Mater. Technol.-Trans. ASME*, 2006, **128**(3), 375-382.

24. A. D. Krawitz, *Mater. Sci. Technol.*, 2011, **27**(3), 589-603.

25. IS0/TTA3: 'Polycrystalline materials – Determination of residual stresses by neutron diffraction', IS0/TTA3, International standardisation organisation, 2001.

26. D. C. I. T. 21432: 'Non-destructive testing. Standard test method for determining of residual stresses by neutron diffraction', DD CEN ISO/TS 21432, British Standards Institute, 2005.

27. M. T. Hutchings, P. J. Withers, T. M. Holden, and T. Lorentzen: 'Introduction to the characterisation of residual stress by neutron diffraction', 424; 2005, Boca Raton, FL, USA, CRC Press.

28. L. Zhang, X. Feng, Z. Li, and C. Liu, *Proceedings of the Institution of Mechanical Engineers, Part B: Journal of Engineering Manufacture*, 2013, **227**(7), 954-964.

29. M. B. Prime, M. A. Newborn, and J. A. Balog: 'Quenching and cold-work residual stresses in aluminium hand forgings: contour method measurement and FEM prediction', THERMEC'2003: Processing & Manufacturing of Advanced Materials, Madrid, Spain, July 7-11, 2003, 2003.

30. D. M. Walker and R. Y. Hom, *Adv. Mater. Process.*, 2002, **160**(6), 57-60.

31. M. Koc, J. Culp, and T. Altan, *Journal of Materials Processing Technology*, 2006, **174**(1-3), 342-354.

32. T. R. Croucher and D. Butler, *Heat Treating*, 1980, **12**(10), 34-37.

33. J. S. Robinson, D. A. Tanner, S. van Petegem, and A. Evans, *Mater. Sci. Technol.*, 2012, **28**(4), 420-430.

34. E. A. Brandes and G. B. Brook: 'Smithells Metals Reference Book'; 2013, Elsevier Science.

35. B. Eigenmann and E. Macherauch, *Materialwiss. Werkstofftech.*, 1996, **27**(10), 491-501.

36. J. W. L. Pang, T. M. Holden, and T. E. Mason, *Acta Mater.*, 1998, **46**(5), 1503-1518.

37. M. B. Prime, T. Gnaeupel-Herold, J. A. Baumann, R. J. Lederich, D. M. Bowden, and R. J. Sebring, *Acta Mater.*, 2006, **54**(15), 4013-4021.

38. 'ASM Speciality handbook', in 'Aluminium and aluminium alloys', (ed. J. R. Davies), 696-698; 1993, ASM International, OH440730002, USA.